JMEPEG
https://doi.org/10.1007/s11665-022-06755-y

1059-9495/$19.00

TECHNICAL ARTICLE

Engineering Framework for Assessing Materials and Processes for In-Space Manufacturing

Harsh G. Bhundiya, Fabien Royer, and Zachary Cordero

Submitted: 6 October 2021 / Revised: 17 January 2022 / Accepted: 20 February 2022

In-space manufacturing is a candidate approach for constructing next-generation space structures with larger characteristic dimensions than modern deployable structures. While many construction methods have been proposed, analysis of their performance for building precision structures, such as large-diameter reflectors, is scarce. In this paper, we present a quantitative, system-level comparison of materials and processes for in-space manufacturing. By using performance metrics for thermal stability, resistance to disturbance loads, and minimal-mass buckling strength, we identify candidate feedstock materials. Then, using the metrics of energy consumption and accuracy, we compare candidate processing methods and find that deformation processing is a promising on-orbit manufacturing method. We synthesize the analysis with a case study on the construction of a tetrahedral truss supporting a reflector surface and provide guidelines for assessing materials and processes for in-space manufacturing.

Keywords deformation processing, in-space manufacturing, material selection, process selection, space structures

1. Introduction

Large space structures have been of interest for decades due to their disruptive potential in space communications (Ref 1, 2), remote sensing (Ref 3), astronomy (Ref 4), power generation (Ref 5), and propulsion (Ref 6). A prime example of the enabling capabilities of large space structures is in remote sensing, where reflectors with diameter greater than 100 meters could dramatically enhance the gain, sensitivity, and spatial resolution of existing systems as well as enable new sensing applications, such as microwave radiometry in geostationary orbit for continuous climate monitoring (Ref 7). Performance benefits are also expected in communications, where larger reflectors could enable higher data rates and smaller ground station antennas (Ref 1); in power generation, where larger support structure could enable MW-scale solar power stations (Ref 8); and in propulsion, where kilometer-scale membranes could enable solar sails to reach previously inaccessible orbits (Ref 6).

This invited article is part of a special issue in the *Journal of Materials Engineering and Performance* entitled "Space and Aerospace Exploration Revolution: Metal Additive Manufacturing." The issue was organized by Shahrooz Nafisi, Relativity Space; Paul Gradl, NASA Marshall Space Flight Center; Douglas Hofmann, NASA Jet Propulsion Laboratory/California Institute of Technology; and Reza Ghomashchi, The University of Adelaide, Australia.

Harsh G. Bhundiya, Fabien Royer, and **Zachary Cordero**, Aeronautics and Astronautics, Massachusetts Institute of Technology, Cambridge, MA 02139. Contact e-mail: zcordero@mit.edu.

Of the many applications of large space structures, precision reflectors have received the most interest because of their practical significance. Multiple structural designs have been proposed and tested for this application, including designs which rely on inflatables (Ref 9, 10), orbital assembly (Ref 11, 12), in-space manufacturing (Ref 13, 14), and deployables (Ref 15-17). The first large inflatable designs to be tested were metallized balloon satellites launched as part of Project Echo in the 1960s (Ref 9). These balloons expanded to a diameter of 30 m and served as passive antennas, successfully reflecting microwave transmissions across North America. Later, the Space Shuttle was used as a platform for demonstrating concepts for in-space assembly (ISA). One such concept proposed using the manipulator arm to assemble small truss modules into a large curved aperture (Ref 11), while another concept relied on astronauts assembling struts into a large mast during extravehicular activities (EVAs). In 1985, in-space manual assembly was first demonstrated when two astronauts assembled a 14-meter long truss outside the Shuttle bay in 25 min (Ref 12). Research into such ISA concepts culminated in the assembly of the largest space structure to date, the International Space Station. Other approaches, known as in-space manufacturing (ISM), considered the use of a robot in space to form feedstock into desired shapes. At the end of the 1970s, two such concepts culminated in ground demonstrations: the Grumman Beam Builder which constructed long metallic trusses by forming and spot-welding thin strips of aluminum (Ref 13); and SCAFEDS which constructed trusses out of a graphite fiber-reinforced plastic by roll forming and ultrasonic welding (Ref 14). Finally, many deployable designs for large antenna reflectors have also been developed. Some examples include the radial-rib antenna, which unfurls similar to an umbrella (Ref 15); the wrap-rib antenna, which deploys by unraveling thin ribs wrapped around a central hub (Ref 16); and the tension truss antenna, which supports a faceted parabolic mesh with tensioned ties (Ref 17).

Despite decades of research on these various approaches to large structures in space, today there are only a few examples of

Published online: 30 March 2022

structures with dimensions greater than 35 m, due to challenges with high costs, complex designs, and performance. For instance, concepts for manual assembly of large trusses were abandoned due to the costs and risks of extended EVAs, such as astronaut fatigue during assembly (Ref 12). Concepts for robotic assembly were not realized due to the low technology readiness level for assembling hierarchical struts and joints (Ref 12). Likewise, concepts for in-space manufacturing were hampered due to the unreliability of manufacturing processes, high energy consumption of operations like welding, and concerns of thermally induced strains during fabrication (Ref 12, 18). While some early deployable and inflatable designs have been adapted for modern reflector antennas, original designs for 100 m-scale structures have been difficult to implement because of issues with the accuracy and reliability of deployment mechanisms (Ref 19), excessive support structure required to survive launch loads, and thermal distortions in the space environment, which cause unwanted surface error and degrade performance. Indeed, modern deployable reflectors exhibit a trade-off between surface precision and diameter, which has limited their practical size to tens of meters (Ref 20).

With this historical backdrop in view, rapidly decreasing launch costs and recent advances in controls and robotics have given rise to resurgent interest in constructing large space structures, especially via ISM. This approach offers the unique opportunity for on-demand fabrication of structures optimized for the space environment. A wide range of construction materials and processing methods have been proposed for ISM. Some examples include: additive manufacturing of hierarchical structures from metallic or fiber-reinforced composite feedstocks (Ref 21, 22); extrusion of fiber-reinforced plastics with high specific stiffness and strength (Ref 23, 24); and deformation processing of complex structures through plastic deformation (Ref 13, 14). However, there has been no systematic comparison of the relative benefits of each approach, making it difficult to determine the optimal ISM approach for a given application.

In this paper, we pursue a system-level comparison between materials and processes in terms of relevant performance metrics for precision space structures like the examples shown in Fig. 1. By using material indices for thermal stability, resistance to disturbance loads, and minimal-mass buckling strength, we identify specific metals, composites, and polymers as candidate construction materials for ISM of such structures. Correspondingly, using the process metrics of energy consumption and accuracy, we compare manufacturing processes amenable to ISM. We then apply these material and process considerations in a case study on ISM of a large tetrahedral truss supporting a reflector surface. This analysis highlights deformation processing as a promising ISM method which has low energy consumption and limited thermal distortion during forming.

2. Material Considerations for ISM

We first identify candidate construction materials for ISM of an exemplar structure: a large curved reflector like the one shown in Fig. 1(b). For such an application, the key design objective is to maintain a specified gain and resolution during the lifetime of the mission. In the space environment, however, there are many sources of inaccuracy which can degrade antenna performance. There are surface distortions from thermal gradients during orbit, which become amplified for larger apertures (Ref 25); there is unwanted deformation from quasi-static and periodic loads, such as from slewing and attitude control (Ref 4); and there are local compressive loads which cause buckling of individual struts (Ref 26). Given these challenges, the optimal design for a reflector antenna would be one in which (1) surface errors from thermal distortion are minimized; (2) surface errors from inertial and periodic disturbances are minimized; and (3) individual members have maximum buckling strength per unit mass. To identify construction materials which satisfy these performance requirements, we use groupings of material properties, termed material indices, originally developed by Ashby and co-workers (Ref 27). These indices serve as quantitative guides in material selection for mechanical design, as optimal materials for a given application are generally those which achieve extremal values of a cost function whose inputs are material indices. In what follows, we use material indices to determine which materials are most suitable for ISM feedstock. Of course, the native performance of structures made from these materials

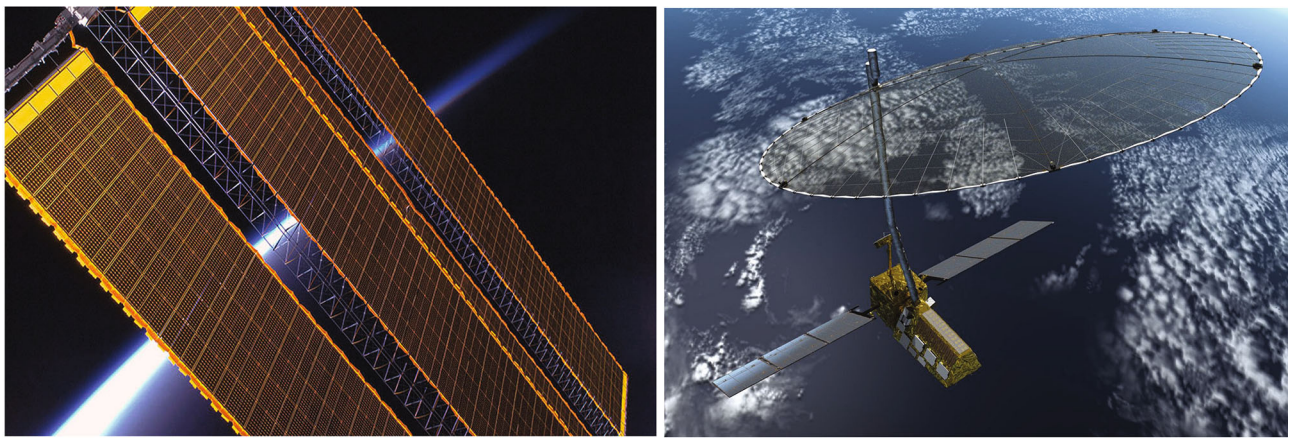

Fig. 1. Exemplar space structures: (a) truss boom supporting the solar panels of the International Space Station (credit: NASA); (b) artist concept of the NISAR spacecraft supporting a large microwave reflector antenna (credit: NASA)

could be enhanced via coatings, active control, and other complementary methods.

2.1 Thermal Stability

Thermal distortions in a large space structure generally result from through-thickness temperature gradients during orbit (Ref 25, 28). To mitigate such distortions, materials must be chosen which have minimal distortion in the presence of a temperature gradient. The relevant material index can be determined by considering a simple conduction model of a simply supported beam of length L and thickness h, heated on one side with a fluctuating heat flux of magnitude q. Assuming the period of fluctuations is greater than the thermal response time of the beam, a steady-state temperature distribution $T(y)$ will develop through the beam thickness. For an unconstrained beam, this will cause a curvature to develop, with magnitude (Ref 29)

$$\kappa = \alpha \frac{dT}{dy} = \frac{\alpha}{\lambda} q. \quad \text{(Eq 1)}$$

Here α is the coefficient of thermal expansion, and Fourier's Law is used to rewrite the temperature gradient in terms of the incoming heat flux q and the beam thermal conductivity λ. By integrating the curvature twice and using simply supported boundary conditions, the central transverse deflection of the beam is obtained as

$$\delta_{max} = \frac{1}{8} q L^2 \left(\frac{\alpha}{\lambda}\right). \quad \text{(Eq 2)}$$

From Eq 2, minimizing the thermal distortion requires maximizing the material index

$$M_1 = \frac{\lambda}{\alpha}. \quad \text{(Eq 3)}$$

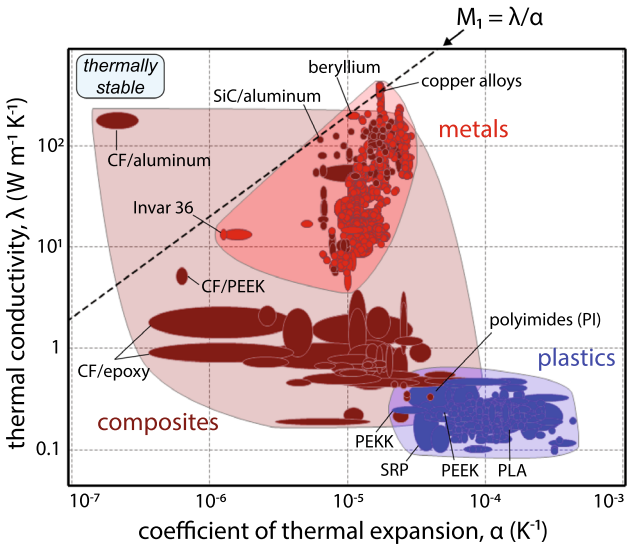

Fig. 2. Material property diagram for selecting ISM feedstock with thermal stability, plotted for three material-classes—metals, polymer/metal–matrix composites, and unfilled plastics (Ref 30). Materials toward the upper left corner are thermally stable and undergo the least distortion in the presence of a through-thickness temperature gradient. Note all material properties are at room temperature.

We seek materials which maximize this performance metric for thermal stability. To this end, Fig. 2 shows the relevant material property diagram, which plots the thermal conductivity λ against the thermal expansion coefficient α for a wide range of ferrous and non-ferrous metals, polymer and metal–matrix composites, and unfilled thermoplastics and thermosets. Figure 2 shows a contour line for the material index M_1 with slope of 1. This line serves as a guide for selecting materials with minimal thermal distortion, and it can be shifted across the plot to identify materials which have the same value of M_1. To select materials which perform best, a line is picked which isolates a search area containing a small number of candidates, as depicted in Fig. 2. Inspection of Fig. 2 shows that among metals, copper alloys, beryllium, and Invar are attractive feedstock materials with minimal thermal distortion. Among composites, the metal–matrix composite of carbon fiber/aluminum is an optimal choice, given its remarkably high thermal conductivity. Other good feedstock candidates are SiC/aluminum, carbon fiber/PEEK, and carbon fiber/epoxy. Comparatively all unfilled polymers have low thermal stability, but among thermoplastics, polyetherketoneketone (PEKK) and self-reinforced polyphenylene (SRP) perform best; and among thermosets, polyimides (PI) perform best.

2.2 Resistance to Disturbance Loads

Next consider the objective of minimizing distortion of a fabricated space structure from disturbance loads. For a large space antenna, unwanted surface error can result when the structure accelerates in response to slewing, attitude control, or gravity gradient loads. If such loads are harmonic, Lake et al. showed that the upper bound on rms surface error (x_{rms}) of a passive structure is given by (Ref 4)

$$x_{rms} \leq \frac{a_{rms}}{4\pi^2 f_0^2}, \quad \text{(Eq 4)}$$

where a_{rms} is the rms magnitude of the accelerations, and f_0 is the fundamental natural frequency of the structure. Equation 4 shows that minimizing surface error from disturbance loads requires maximizing the fundamental natural frequency of the structure. Modeling the aperture of a space antenna as a flat, isotropic circular plate with fixed diameter and bending stiffness but varying depth, the relevant material index which maximizes its natural frequency is (Ref 29)

$$M_u = \left(\frac{E^{1/3}}{\rho}\right)^{1/2}. \quad \text{(Eq 5)}$$

The above material index, a function of the Young's modulus E and density ρ, does not consider damping, as it assumes the harmonic loads do not excite the natural frequencies of the structure. However, if the excitation covers a wide frequency range which includes the resonant frequencies of the structure, damping becomes important. In that case, a relevant material index can be derived by considering the passive damping of the feedstock through the material loss coefficient η (Ref 29). The resulting material index is

$$M_2 = \eta M_u^{k-1}, \quad \text{(Eq 6)}$$

where the constant k (typically greater than 2) describes the power spectral density of the excitation. In particular, $k = 2$ represents a disturbance with constant input velocity and finite power; $k > 2$ represents an excitation more concentrated at low

frequencies; and $k \to \infty$ represents a disturbance that does not excite any resonant frequencies. In this way, the constant k represents the relative importance of the material damping η to the material index for maximizing natural frequency M_u. The smaller the value of k, the closer the excitation to the resonant frequencies and the more important the inherent damping. Note that Eq 6 only considers passive damping of the feedstock. For a large structure, the damping from mechanical interfaces and the resulting interface friction will ultimately contribute greater damping which is not considered by this simplified material index. Nonetheless, a larger value of k can represent the increased importance of maximizing natural frequency in such cases.

To identify materials which maximize this performance metric for minimal distortion, we plot the relevant material property diagram in Fig. 3. Here the material index M_u, which represents the maximum natural frequency achievable for a flat plate, is plotted against the material loss coefficient η, a measure of energy dissipated per loading cycle. To guide material selection, a contour line for M_2 with a slope of $1/(1-k)$ is overlaid. Here we use a value of $k = 2$, corresponding to a disturbance with finite power and a scenario where material damping is as important as maximizing the natural frequency.

In Fig. 3, optimal feedstock materials are located near the upper right corner, as they offer great damping as well as a high natural frequency which minimizes distortion. The chart shows an inverse trend between loss coefficient η and the material index M_u. Thus, identifying an ISM feedstock material which minimizes distortion from disturbances represents a tradeoff between damping and stiffness. Compliant plastics like PVC and ethylene ethyl acrylate (EEA) offer great passive damping but lack stiffness, while stiff composites like carbon fiber/cyanate ester and carbon fiber/PEEK create structures with high natural frequency but poor damping. This contrast is magnified by the thermal stability considerations of the previous subsection: Monolithic plastics have high thermal expansion and temperature-sensitive damping, while high-performance composites are thermally stable. Given these trends, maximizing the material index for resistance to disturbances suggests selecting feedstock materials which have relatively high values of both η and M_u, such as the thermoplastic PLA, the thermoset vinyl ester (VE), or 300-series aluminum alloys. However, if the chief concern is disturbances at low frequencies where damping is not vital, using a composite material like CFRP is an optimal choice.

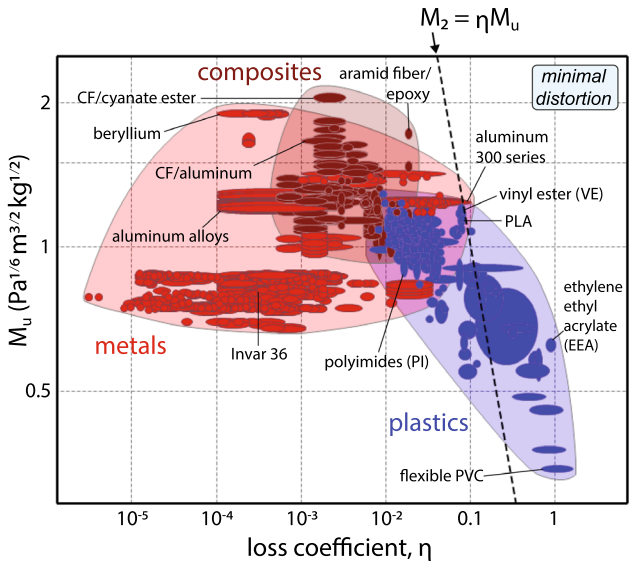

Fig. 3. Material property diagram for selecting ISM feedstock with minimal distortion from harmonic disturbance loads, plotted for the same materials as Fig. 2 (Ref 30). Structures fabricated with materials toward the upper right corner have minimal distortion due to both high damping and high natural frequency. A trade-off between damping and stiffness is observed.

2.3 Minimal-Mass Buckling Strength

Lastly consider the objective of selecting ISM feedstock which maximizes buckling strength per unit mass of a space structure. Assuming the structure comprises slender members which support fixed compressive loads without buckling, the mass of each member is minimized if the selected material maximizes the index (Ref 27)

$$M_3 = \frac{(\phi_{\max} E)^{1/2}}{\rho}. \qquad \text{(Eq 7)}$$

Here E is the Young's modulus, ρ the density, and $\phi_{\max}$ the maximum achievable shape factor of the cross section, approximated as (Ref 27)

$$\phi_{\max} \approx 2.3\left(\frac{E}{\sigma_f}\right)^{1/2}, \qquad \text{(Eq 8)}$$

where σ_f is the tensile strength of the material. Note that Eq 8 assumes that each member has a cross section optimized for buckling with matching local and global buckling loads.

Figure 4 shows the relevant material property diagram for this index, where Young's modulus is multiplied by the dimensionless shape factor given in Eq 8 and plotted against density for the same three material classes as above. A contour line for M_3 with a slope of 2 is overlaid to guide material selection for this index. Among metals, beryllium and its alloys

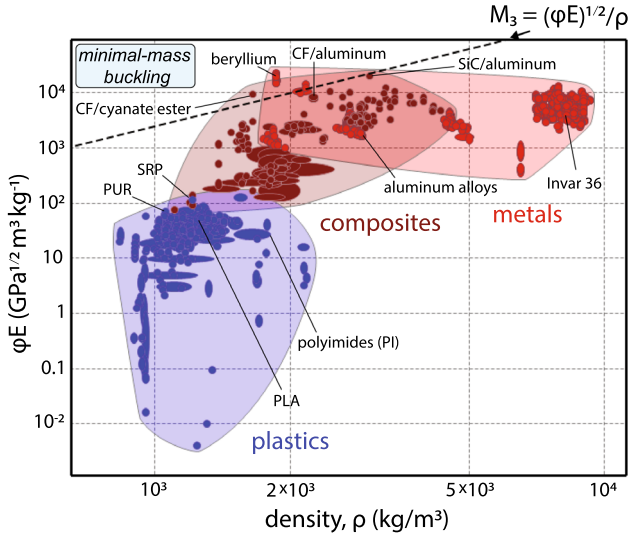

Fig. 4. Material property diagram for selecting ISM feedstock with minimal-mass buckling strength, plotted for the same materials as Fig. 2 (Ref 30). Materials in the upper left corner are optimal for buckling due to their superior combination of Young's modulus, tensile strength, and density.

Table 1. Candidate ISM feedstock materials for optimizing performance of a large space structure, particularly thermal stability, resistance to disturbance loads, and minimal-mass buckling strength. Materials which maximize the listed material indices are highlighted in bold

		Thermal stability	Resistance to disturbance loads		Minimal-mass buckling
		$M_1 = \lambda/\alpha$ $[\mathrm{MW/m}]$	η $[10^{-3}]$	$M_u = \left(E^{1/3}/\rho\right)^{1/2}$ $[\mathrm{Pa^{1/6}m^{3/2}kg^{-1/2}}]$	$M_3 = (\varphi E)^{\frac{1}{2}}/\rho$ $[\mathrm{kPa^{1/2}m^3kg^{-1}}]$
Metals	Al alloys	10.7	2	1.25	20
	Beryllium	20.6	1	1.92	**82**
	Cu alloys	23.6	1	0.75	9
	Invar	26.9	0.5	0.8	9.1
Composites	**CF/Al**	**1230**	3	1.69	41
	CF/cyanate ester	0.163	3.3	**2.1**	59
	CF/epoxy	5.1	3.3	1.85	34
	CF/PEEK	10.3	3.3	1.85	33
Plastics	Polyimides (PI)	0.018	16.4	0.95	3.2
	PLA	0.0013	80	1.11	6.1
	PVC	0.0016	**1600**	0.35	0.1
	Self-reinforced polyphenylene (SRP)	0.01	9.2	1.3	9.1

are optimal ISM feedstock materials for minimal-mass buckling, due to their high specific stiffness and strength. Among composites, carbon fiber-reinforced thermosets and aluminum–matrix composites offer similar performance. While unfilled plastics are generally less efficient for buckling, thermoplastics like self-reinforced polyphenylene (SRP) and thermosets like polyurethane (PUR) appear to be fair feedstock candidates.

3. Summary

Figures 2, 3 and 4 suggest selecting different feedstock materials for in-space manufacturing of a large structure based on its performance objectives: high- λ metals and low- α composites for thermal stability; plastics and composites for minimizing surface error from disturbances; and metals and composites for minimal-mass buckling strength. To better understand which materials are optimal for each objective, material index values for promising feedstock candidates from each material class are listed in Table 1.

The above analysis highlights the following takeaways. First, no one feedstock material is optimal for all performance objectives of a large space structure. While carbon fiber-reinforced aluminum and Invar have excellent thermal stability, they are not optimal for minimal distortion or buckling strength. This suggests that the ideal ISM process is one which can fabricate structural members from all three material classes, thereby leveraging the unique properties of each. Second, Figs. 2, 3 and 4 highlight the tradeoff between material properties of stiffness and damping. While CFRPs have great specific stiffness and result in structures with high natural frequency, a large structure built from such a material would be vulnerable to disturbances due to relatively low passive damping. Hence, selecting and developing ISM feedstocks with damping are important, particularly for large space structures. Lastly, we verify our simple analysis by noting that the material candidates in Table 1 are indeed used in space applications today. The hexagonal mirror segments of the James Webb Space Telescope, for instance, are constructed from beryllium due to its high flexural stiffness and stability at cryogenic temperatures (Ref 31). Deployable booms, routinely used for deploying optics, solar arrays, and solar sails (Ref 32-34), are constructed from CFRPs due to their high specific stiffness. And metal-matrix composites such as SiC/aluminum are used to fabricate precision space optics due to their damping properties and stiffness at elevated temperatures (Ref 35). In this way, the three presented material indices serve as guidelines when selecting feedstock for manufacturing precision space structures. Additionally, this analysis guides future development of ISM feedstocks, such as high-performance composites with larger loss coefficients which are better suited to handle disturbance loads in space.

4. Process Considerations for ISM

Having identified candidate feedstock materials for ISM in Section 2, we now compare several processes, amenable to these different materials, which have shown promise as potential manufacturing methods in space. These include: melt-based additive manufacturing (AM) of metals and plastics, extrusion of fiber-reinforced polymers, and deformation processing of metals. These processing approaches have been pursued to varying levels of maturity (Ref 21-24). NASA, for instance, has developed a metal additive manufacturing process which melts wire feedstock onto a substrate via an electron beam (Ref 21). This process has been demonstrated via ground-testing with Al-, Ti-, Ni-, and Fe-based alloys and in microgravity with an Al alloy, at a build rate of 4.5 kg/h and a nominal power draw of 10 kW. Another example of melt-based AM is the process reported by Redwire Space, which uses fused-deposition modeling to fabricate beams from carbon fiber-reinforced thermoplastic polymers (Ref 22). This process will soon be demonstrated in space with the fabrication of two 10-m-long beams, as part of the NASA OSAM-2 mission (Ref 36). Additionally, Tethers Unlimited has developed an extrusion-based process which fabricates trusses from comingled yarn of carbon fiber and PEEK. During a ground demonstration

in 2018, this process fabricated a 10-m-long triangular boom at a build rate of 0.1 kg/h and nominal power draw of 100 W (Ref 23). Finally, Kleos Space has reported a pultrusion-based process to construct beams from a thermoset plastic reinforced by continuous carbon fibers (Ref 24).

To compare these various ISM processes, we use two performance metrics important for constructing precision space structures, namely the specific energy consumption and the achievable accuracy. Given power constraints, the energy consumption is directly tied to the build rate: For a spacecraft with fixed power output P, the build rate $\dot{m}$ of an arbitrary structure is

$$\dot{m} = P/u, \tag{Eq 9}$$

where u is the specific energy consumption of the manufacturing process. Hence, ISM processes with lower energy consumption can achieve faster build rates, thereby mitigating issues with stability and thermal management during fabrication on orbit. The second metric for comparison is the process accuracy, which affects the performance of space structures through fabrication tolerances of each member. If an ISM process can maximize accuracy, fabricated structures such as curved reflectors and truss booms can achieve maximal gain and tip accuracy.

4.1 Energy Required

Given that energy consumption varies greatly with machine parameters and process details, we present here an order-of-magnitude comparison of the minimum energy required for the three ISM processes identified above—melt-based additive manufacturing, extrusion of fiber-reinforced composites, and deformation processing—based on the physics of their primary shaping mechanisms. This discussion follows closely that presented by Ashby in Ref 27 on energy-efficient material processing.

The first process, melt-based processing of metals and plastics, requires melting of feedstock before depositing onto a build platform. In extrusion methods like fused-deposition modeling (FDM), melting is achieved through heating of the nozzle, while for directed-energy-deposition (DED) and powder-bed-fusion (PBF) methods, it is achieved by a laser or electron beam. Given the common processing step of melting, we estimate the minimum energy per unit mass as the sum of the energy required to reach the melting temperature and the latent heat of melting, expressed as (Ref 27)

$$u_{\text{melt}} = C_p(T_m - T_0) + L_m, \tag{Eq 10}$$

where C_p is the specific heat, T_m the melting temperature, T_0 the ambient temperature, and L_m the latent heat. Assuming the feedstock material is heated in space from a low ambient temperature, $T_m \gg T_0$. Furthermore, using the approximate correlation $L_m \approx 0.4 C_p T_m$ and an overall process efficiency of 15% to account for heat losses (Ref 27, 37), the required process energy per kilogram is approximately

$$u_M^* \approx 9.3 C_p T_m. \tag{Eq 11}$$

Note that Eq 11 only considers the energy required for melting, as it is the primary shaping mechanism of melt-based additive manufacturing. We do not include the energy required for secondary processing steps, such as feeding material into the nozzle/build tray or moving the nozzle around the build platform, as these steps generally require a relatively small fraction of the total energy (Ref 38).

Similar to melt-based processes, extrusion of fiber-reinforced polymers in space requires heating of feedstock close to its melting point. However, in this case the feedstock is heterogenous, and its specific heat (C_{FRP}) is given by the rule of mixtures,

$$C_{FRP} = w_f C_f + (1 - w_f) C_m, \tag{Eq 12}$$

where w_f is the weight fraction of the fiber, and C_f, C_m are the specific heats of the fiber and matrix, respectively (Ref 39). Additionally, the processing energy differs between thermoplastic and thermoset matrices. Extrusion of fiber-reinforced thermoplastics relies on heating the matrix beyond its glass transition temperature before it is cooled in the desired shape, while extrusion of fiber-reinforced thermosets relies on a chemical curing reaction which causes permanent polymerization and cross-linking. Hence, we consider each scenario separately. In the case of a thermoplastic matrix, we estimate the energy required to heat the polymer matrix to its melting temperature, with a process efficiency of 15%,

$$u_{FRP-TP}^* \approx 9.3 C_{FRP} T_m. \tag{Eq 13}$$

Here, C_{FRP} is the specific heat of the composite, and T_m is the melting temperature of the thermoplastic matrix.

For thermoset matrices, we derive a different expression based on the curing reaction. While the curing is generally exothermic, it requires an activation energy input in the form of heat or pressure. For extrusion of complex shapes, the thermoset matrix is also heated to allow its flow into a shaping tool and proper wetting of the fibers. While these steps do not require complete melting of the matrix, they require, in most cases, heating of the matrix to its glass transition temperature, T_g. Thus, we estimate the process energy per unit mass as the energy required to heat the composite to the glass transition temperature of the matrix. Using a process efficiency of 15%, we obtain

$$u_{FRP-TS}^* \approx 6.7 C_{FRP} T_g, \tag{Eq 14}$$

where C_{FRP} is the specific heat of the composite.

Equations 13 and 14 do not consider secondary shaping steps specific to extrusion of composites, such as pulling of the feedstock through a die to achieve the desired cross section. The mechanical work per unit mass for such a step can be approximated as

$$u_{\text{mechanical}} \approx \frac{\mu}{\rho}\dot{\epsilon}, \tag{Eq 15}$$

where μ is the dynamic viscosity of the matrix near its melting temperature, ρ the density of the composite, and $\dot{\epsilon}$ the strain rate during deformation. To compare the relative magnitude of this mechanical work with the energy required for heating the feedstock, we consider an exemplar extrusion process which uses a conical die to decrease the cross-sectional area of the heated material. In this case, the strain rate is approximated as (Ref 40)

$$\dot{\epsilon} \approx 6v\left(\frac{d_o^2}{d_o^3 - d_f^3}\right)\ln\left(\frac{d_o^2}{d_f^2}\right), \tag{Eq 16}$$

where v is the velocity of extrusion and d_o, d_f are the initial and final diameters of the extrudate, respectively. Using

representative values of $d_o = 5$ cm, $d_f = 2.5$ cm, and $v = 5$ cm/min, the strain rate is approximately $\dot{\epsilon} \approx 0.16$ s^{-1}. Then, assuming a 15% process efficiency and using a typical melt viscosity of $\mu = 3 \times 10^4$ Pa · s and a density of $\rho = 1600$ kg/m^3, for PEEK reinforced with 60% carbon fibers by volume (Ref 41), we obtain the following estimate of the mechanical work per kilogram:

$$u_{\substack{\text{mechanical,} \\ \text{CF/PEEK}}} \approx 20.1 \text{ J/kg}.$$

We can compare this value with the energy required for heating the CF/PEEK composite to the melting point of the matrix, obtained from Eq 13, using $w_f = 0.6$, $C_f = 715$ J/(kg · K), $C_m = 1340$ J/(kg · K), and $T_m = 380$°C:

$$u_{\substack{\text{heating,} \\ \text{CF/PEEK}}} \approx 3.4 \text{ MJ/kg}.$$

The energy required for heating the CF/PEEK composite is thus orders of magnitudes larger than the mechanical work during extrusion. This result also holds for a composite with a thermoset matrix. The above calculation supports our assumption that the majority of energy required for extrusion of fiber-reinforced plastics goes into heating the feedstock, which can be approximated with Eq 13 and 14.

The third ISM processing technique, deformation processing, does not rely on heating of feedstock but instead on plastic deformation to achieve the desired shape. To estimate the energy required for this process, we assume an average flow stress of $(\sigma_y + \sigma_{uts})/2$ and a strain of order 1. Dividing the resulting strain energy by the density of the material, and using an efficiency of 15%, the energy required to deform a material per unit mass is given by (Ref 27)

$$u_D^* \approx 3\frac{\sigma_y + \sigma_{uts}}{\rho}. \qquad \text{(Eq 17)}$$

By only considering the mechanical work from plastic deformation, Eq 17 does not consider the energy for any secondary processing steps, such as feeding or straightening the material.

Using the expressions developed above, Fig. 5 compares the energy requirements for melt-based processing, extrusion of fiber-reinforced plastics, and deformation processing for a range of possible ISM feedstock materials. The energies required for melt-based and deformation processing, given by Eq 11 and 17, are plotted for unfilled plastics and ferrous/non-ferrous metals. The energies required for extrusion of fiber-reinforced plastics, given by Eq 13 and 14, are plotted for both thermoplastic and thermoset matrices reinforced with 50% carbon fibers by weight.

Figure 5 shows that, out of the three processes under consideration, melt-based processes require the greatest energy per unit mass, around 8 MJ/kg for most metals and between 5 and 8 MJ/kg for most plastics. Extrusion of carbon fiber-reinforced thermoplastics and thermosets requires less energy, between 3 and 6 MJ/kg, due to the lower specific heat of the composite feedstock and lower heating requirements. Comparatively, deformation processing of metals and plastics requires the least specific energy, between 0.1 and 2 MJ/kg for metals and 0.05-1 MJ/kg for plastics, which is expended only on plastic deformation. This comparison of approximate energy consumption is directly tied to the maximum build rates of the ISM processes, given by Eq 9. Using the specific energies of Fig. 5 and assuming a medium-sized spacecraft with 1 kW power output (i.e., from commercially available solar panels), we find that an ISM process which melts metals or plastics can achieve build rates up to 0.72 kg/h; one which extrudes fiber-reinforced plastics can achieve up to 1.2 kg/h; and one which deforms metals or plastics can achieve up to 36 kg/h. This comparison highlights the relatively low energy requirements of deformation processing compared to other processes which rely on material heating. While the assumed efficiencies of 15% may differ in actual processes, it suggests that if limited by energy consumption, the fastest ISM process relies on deformation processing for shaping feedstock.

While the above analysis is approximate, the calculated process energies of Fig. 5 compare favorably with the energy consumption of prototype ISM systems which have been ground-tested. The metal additive manufacturing system developed by NASA (Ref 21), for instance, has fabricated aluminum parts at a build rate of 4.5 kg/h and power draw of 10 kW, yielding a specific energy of 7.9 MJ/kg, a value which matches the energy for melt-based processing in Fig. 5. Similarly, the extrusion-based process reported by Tethers Unlimited (Ref 23) has constructed trusses from CF/PEEK at a build rate of 0.1 kg/h and power draw of 100 W, placing it at 3.6 MJ/kg, a value which matches the calculated energy range for extrusion of thermoplastics. Lastly, the exemplar deformation process of Bend-Forming (which forms wire feedstock into trusses as described in Ref 42) can achieve a build rate of a 0.27 kg/h and power draw of 25 W, placing it at 0.33 MJ/kg, which too matches the calculated energy range in Fig. 5.

The above comparison motivates deformation processing as a relatively low-energy and fast manufacturing method, but it does not consider material compatibility with the process. One such issue is the tendency of brittle feedstock to fracture during forming, which prevents the use of metals like beryllium or composites like CF/PEEK and SiC/aluminum, which have low strain to failure (around 1%). Ductile metals and polymers, such as steels, aluminum alloys, and polyesters, are more suitable to plastic deformation as they can achieve greater than

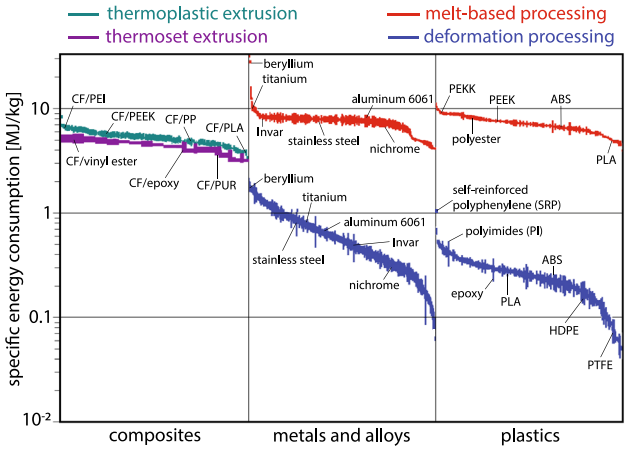

Fig. 5. A comparison of specific energy consumption for three ISM processing methods: melt-based processing, extrusion of carbon fiber-reinforced thermoplastics/thermosets (with 50% fiber weight fraction), and deformation processing (Ref 30). Each process is represented by a different color, and its specific energy consumption is plotted for relevant feedstock materials, including composites, metals, and plastics. For many materials, the energy consumption of deformation processing is the lowest.

10% strain to failure. Furthermore, hybrid feedstock materials in which ductile and brittle constituents are selectively patterned to achieve functionally graded ductility may be amenable to processes with localized plastic deformation.

4.2 Accuracy

A second key performance metric for an ISM process is accuracy, which is of critical importance for fabrication of structures such as curved reflectors for space antennas and telescopes, whose performance requires minimal surface error (Ref 25). While the accuracy of different manufacturing processes can be difficult to compare as it depends on the tolerances of individual steps and the geometry of the final structure, in this section we highlight factors which limit the accuracy of the three ISM processes under consideration, focusing on factors unique to the space environment. We also suggest strategies to minimize distortion in space, without considering a particular structural geometry. Note that for specific space structures such as a truss-supported reflector, frameworks exist for predicting surface distortion from fabrication errors like member length deviations (Ref 43).

For terrestrial structures fabricated with AM, key factors which limit the dimensional accuracy include layer heights, residual thermal stresses, and positional tolerances of the nozzle and laser/electron beam (Ref 44, 45). In the space environment, additional considerations are necessary. For instance, the lack of convective cooling and the presence of solar heating may magnify thermal stresses during fabrication and cause degradation of mechanical properties. While in terrestrial manufacturing, the volumetric shrinkage during solidification may be mitigated by stress relief annealing of the part and build plate, it is unclear how to accomplish something similar in space. Furthermore, microgravity will affect the adhesion of feedstock to previously built layers by eliminating body forces and increasing the dominance of surface tension-driven capillary forces. Indeed, aluminum prototypes built in microgravity by the metal additive manufacturing system developed by NASA have shown uneven layer heights due to such adhesion issues (Ref 46). The experiments also showed issues like balling of molten material at the end of the wire feedstock, which inhibited metal transfer and resulted in an uneven build surface. Such challenges, unique to the space environment, need to be considered for an ISM process which relies on melt-based AM.

For extrusion of fiber-reinforced plastics under gravity, inaccuracies can result from non-uniformity of heating, viscous flow under gravitational body forces, and positional tolerances of the nozzle and die (Ref 47, 48). In space, microgravity might alleviate some challenges, such as distortion of the extrudate during curing (Ref 49). However, achieving uniform heating in space may be difficult given varying solar heat fluxes and thermal radiation. For thermoset polymer matrices, this can give rise to distortion from nonuniform shrinkage during curing, particularly if the structure has not fully cured before exiting the nozzle. To illustrate this challenge, we present a thermomechanical finite element model of a fiber-reinforced thermosetting beam extruded into space. The model setup is shown in Fig. 6: A tube of length $L = 1$ m, with outer radius $R = 0.02$ m and wall thickness $t = 0.001$ m, is extruded with velocity v into the space environment. The extrusion is simulated with moving temperature and displacement boundary conditions on the outer surface of the tube. Inside the nozzle, the tube is held rigid and at an initial temperature T_0; after extrusion, the tube is free to deform, radiates to an ambient temperature of 3 K, and is subject to solar heating of 1360 W/m^2 on its top surface. The model, implemented in the COMSOL Multiphysics software (Ref 50), accounts for curing kinetics of the thermoset matrix, heat transfer, and solid mechanics, following the analytical model presented in Ref 51 for curing shrinkage of a carbon fiber-reinforced epoxy composite (CYCOM 5320-1). In our model, we assume that the tube is made of the same material, with stacked unidirectional plies along the extrusion axis. Hence, we use expressions for the orthotropic elastic constants, thermal expansion coefficients, and chemical shrinkage coefficients obtained for a unidirectional ply in Ref 51. Other material properties used in the model are listed in Table 2. Note that while the model presented in Ref 51 was derived for a curing cycle at constant temperature, we use the same model to calculate deformation under varying heat flux and radiative boundary conditions which simulate the space environment.

Each simulation starts with the tube at a uniform temperature of T_0 and a uniform degree of cure (ξ) of $\xi_0 = 0.38$, which represents the gelation point of the epoxy resin. Then, the moving temperature boundary condition is implemented at velocity $v = 5$ mm/s, and the governing differential equations are solved for the temperature, degree of cure, and displacement at each node along the tube. With a simulation time of 800 s, the tube is fully extruded in the first 200 s and subsequently subject to only the temperature boundary conditions of the space environment.

Figure 7(a)-(c) plots the evolution of the average surface temperature, average surface degree of cure, and tip displacement as functions of time for an initial nozzle temperature of $T_0 = 450$ K. We see that during and after extrusion, the mean and maximum temperatures of the tube increase due to solar heating, while the minimum temperature decreases due to radiation into space. The resulting temperature and degree of cure distributions are non-uniform across the cross section and give rise to transverse deflection of up to 4 mm via both thermal expansion and chemical shrinkage. Figure 7(d)-(f) plots the temperature, degree of cure, and displacement of the tube at the end of the simulation. Although none of the three dependent variables reach steady-state values after 800 s, the top surface fully cures and reaches a temperature of 650 K, while the bottom surface only cures to $\xi = 0.46$ and is roughly 280 K cooler. The lower temperature on the bottom surface causes slower curing kinetics, ultimately giving rise to distortion from uneven curing.

To deconvolute the effects of non-uniform cure and temperature gradients across the cross section, Fig. 8 shows the average curvature of the tube from thermal expansion and chemical shrinkage separately. For comparison, we also overlay approximate expressions for the two curvatures, given by

$$\kappa_{TE} = \frac{1}{h}[\alpha_1(T_t - T_b)], \quad \text{(Eq 18)}$$

$$\kappa_{CS} = \frac{1}{h}[\beta_1(\xi_t - \xi_b)]. \quad \text{(Eq 19)}$$

Here h is the thickness of the extruded profile (i.e., tube diameter); α_1, β_1 are the coefficients of thermal expansion and chemical shrinkage along the extrusion direction (i.e., coincident with fiber direction); T_t, T_b are the average temperatures of the top and bottom surfaces; and ξ_t, ξ_b are the average degrees

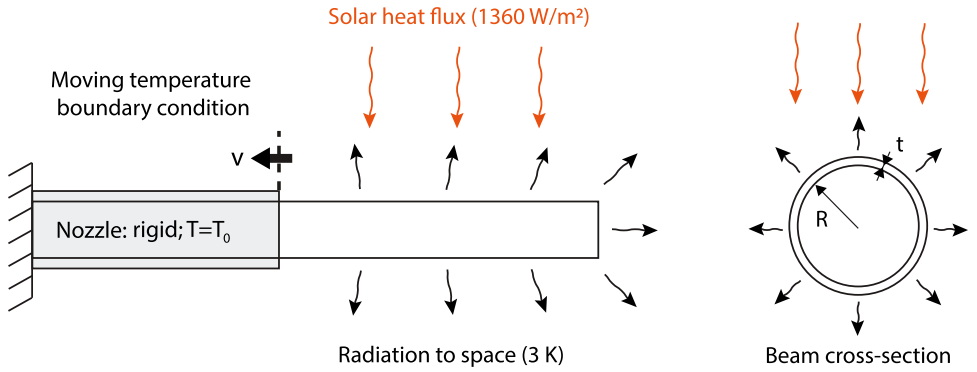

Fig. 6. Model setup of a thermomechanical simulation of an extruding CF/epoxy tube in space. Extrusion is simulated with a moving temperature boundary on a fixed-length beam. On the one side of the boundary, the tube is rigid and at fixed temperature; on the other side, it is subject to temperature boundary conditions which simulate the space environment.

Table 2. Material properties used for the exemplar CF/epoxy composite CYCOM 5320-1. The density (ρ), specific heat (C_p), and longitudinal, transverse thermal conductivities (k_1, k_2) are obtained via rule of mixtures. The heat of the reaction (H_r) is used as an exothermic heat source during curing. All other orthotropic elastic constants are obtained from Ref 51

ρ, kg/m^3	C_p, kJ/(kg · K)	k_1, W/(m · K)	k_2, W/(m · K)	H_r, kJ/kg,
1588	0.871	5.88	0.46	500

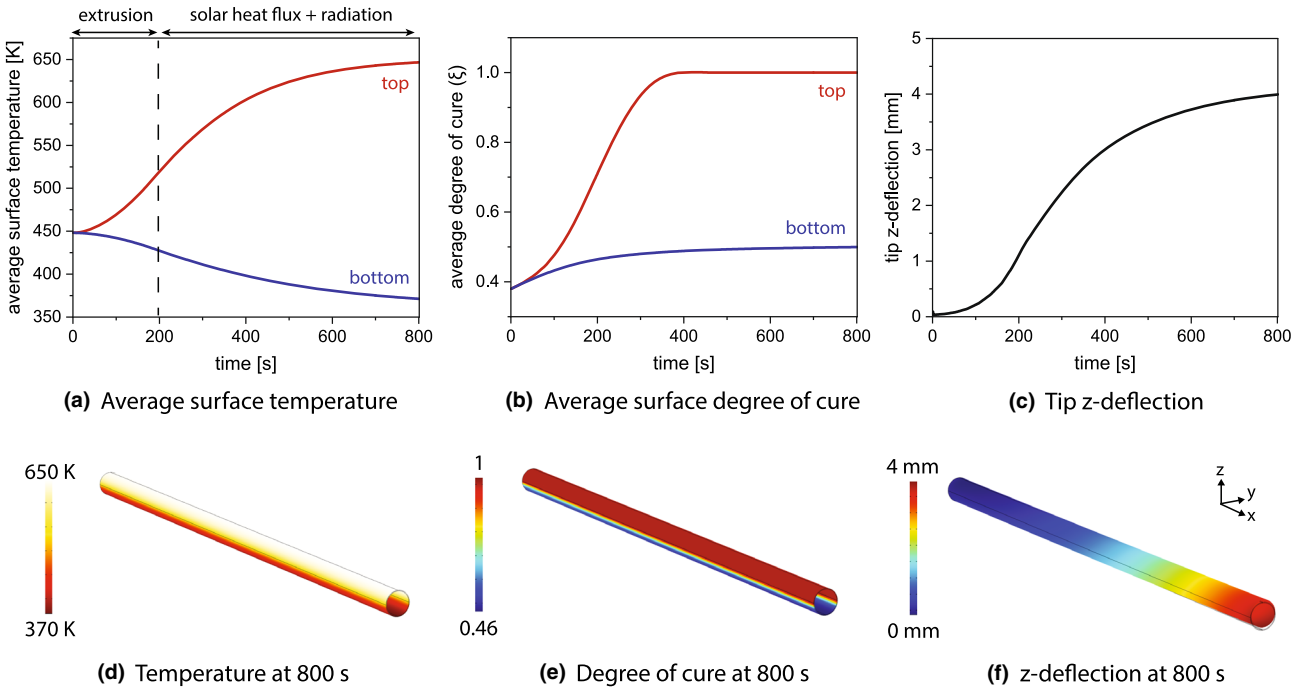

Fig. 7. Simulation results for extrusion of a partially cured CF/epoxy tube into space, modeled with the COMSOL Multiphysics software (Ref 50). The extrusion velocity, nozzle temperature, and initial degree of cure are $v = 5$ mm/s, $T_0 = 450$ K, and $\xi_0 = 0.38$, respectively. The extrusion is modeled for the first 200 s; afterward, the tube is subject to solar heat flux on its top surface and radiation to a low ambient temperature. (a)-(c) plot the average surface temperature, average surface degree of cure, and tip deflection as a function of time, while (d)-(f) show their distributions along the tube at the end of the simulation. Gradients in temperature and degree of cure across the cross section cause deflection at the tip.

of cure of the top and bottom surfaces, respectively. In Fig. 8, we plot Eq 18 and 19 as functions of time by substituting the average surface temperatures and degrees of cure of the CF/epoxy tube from Fig. 7(a)-(b) and the approximate values $\alpha_1 = -0.96 \times 10^{-6}$ K^{-1}, $\beta_1 = -25 \times 10^{-6}$ obtained for a unidirectional ply in Ref 51.

Figure 8 shows that the majority of the tube curvature is due to the thermal expansion of the CF/epoxy material, almost an

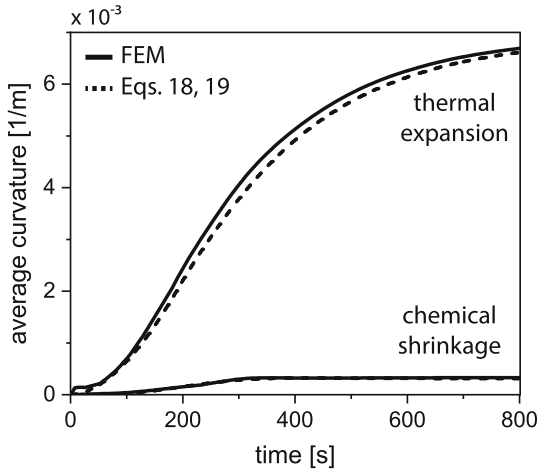

Fig. 8. Evolution of curvature in an extruding CF/epoxy tube from thermal expansion and chemical shrinkage, separately

order of magnitude greater than that from chemical shrinkage. Nonetheless, for different composite materials with larger chemical shrinkage coefficients, the distortion due to chemical shrinkage may become significant and impact the accuracy. For instance, while the epoxy modeled here has a chemical shrinkage coefficient of $\beta = 0.022$, other bisphenol epoxies have been measured to have shrinkage coefficients of $\beta = 0.095$ (Ref 52), a difference which would increase the magnitude of chemical shrinkage strains. In addition, while our model considered a CF/epoxy tube with circular cross section, chemical shrinkage may dominate distortion for laminates with L-cross section (Ref 53), as there are additional couplings between in-plane and out-of-plane strains. Hence, Fig. 8 suggests that both thermal expansion and chemical shrinkage are important sources of distortion during extrusion in space, and their magnitudes can be approximated well with Eq 18 and 19. From these expressions, we see that the distortion can be minimized by choosing feedstock with high transverse thermal conductivity and low longitudinal thermal expansion/chemical shrinkage coefficients. Given the difference in thermal properties of the carbon fibers and polymer matrix, this suggests selecting feedstock material with high fiber volume fraction and aligning fibers with the extrusion axis.

The evolution of degree of cure after the tube exits the nozzle suggests that distortion can be minimized by tailoring extrusion rate and nozzle temperature such that the degree of cure of the cold surface is close to that of the hot surface. To understand the effect of the nozzle temperature T_0 on the extrusion of the tube, we conduct identical simulations with $v = 5$ mm/s and $\xi_0 = 0.38$, but for the range of nozzle temperatures: $T_0 = 450\ \text{K}, 475\ \text{K}, 500\ \text{K}$. The resulting changes in average surface temperatures, surface degrees of cure, and curvature of the CF/epoxy tube are shown in Fig. 9. The plots show that increasing T_0 decreases the gradient in ξ across the cross section of the tube, resulting in smaller curvature after 800 s. These simulations suggest that ISM processes with higher nozzle temperatures may minimize distortion from thermal expansion and uneven curing in space.

The discussion above highlights challenges with maintaining accuracy in ISM techniques which rely on large thermal excursions, as in melt-based processing of metals, or precisely controlled thermal environments, as in extrusion processing of thermoset materials. Importantly, since deformation processing of certain ductile materials does not require elevated temperatures, this process might be less sensitive to the unique thermal environment of space. The primary source of inaccuracy in deformation processing is elastic springback, which is controlled by the shape, stiffness, and strength of the feedstock as well as the bend radius of the tool (Ref 54). In conventional deformation processing, springback is mitigated through calibration experiments or through process modifications which give more spatially uniform plastic strains (e.g., stretch forming). Because stiffness and strength can vary with temperature, achieving high accuracy via deformation processing in space would require calibrating springback over the thermal cycle expected on orbit.

5. Material and Process Selection Case Study: ISM of a Tetrahedral Truss

We next synthesize the material and process selection considerations of Sections 2 and 4 in a case study: in-space manufacturing of a tetrahedral truss supporting a reflector surface, as illustrated in Fig. 10. We contrast various materials and ISM processes for constructing this truss structure with three performance metrics, namely the truss mass M_t, the truss fundamental natural frequency f_0, and the total build time t. For applications such as support structure for a space telescope, a small truss mass, high natural frequency, and fast build times are generally desired, to maximize structural efficiency of the truss and minimize thermal effects during fabrication. Here we focus on a specific truss geometry with a depth-to-diameter ratio of 0.2 and derive expressions for M_t, f_0, and t as a function of diameter for various strut feedstock materials and processing methods. We choose this particular depth-to-diameter ratio as it results in an efficient truss geometry with minimal truss mass fraction. We assume a reflector surface with an areal density of $\rho_A = 18\ \text{kg/m}^2$, which corresponds to the beryllium mirrors of the James Webb Space Telescope (Ref 55).

Following the analysis of Lake et al. (Ref 4), summarized in Appendix A, we compute the mass and fundamental frequency of a tetrahedral truss with a strut radius of $r = 5$ mm. Figure 11 plots the two variables as a function of truss diameter between 10 m and 100 m, for five candidate feedstock materials selected from Table 1. Note that here we assume the strut radius remains constant as the truss diameter increases; other strut radii may be considered for specific applications.

We see from Fig. 11(a) that using CFRP feedstocks yields tetrahedral trusses with the lowest mass, ranging between 25 kg and 250 kg for the range of diameters considered. Trusses constructed from carbon fiber-reinforced aluminum are second in performance, as their mass stays between 45 kg and 460 kg. Comparatively, heavier feedstock materials like aluminum alloys and Invar yield masses are approximately an order of magnitude larger, up to almost 1700 kg for the largest structures considered. This material comparison is also reflected in the evolution of fundamental natural frequency in Fig. 11(b): composite feedstock materials yield trusses with higher natural frequency than metals. Note that the comparative performance of Invar and aluminum alloys is reversed for the frequency

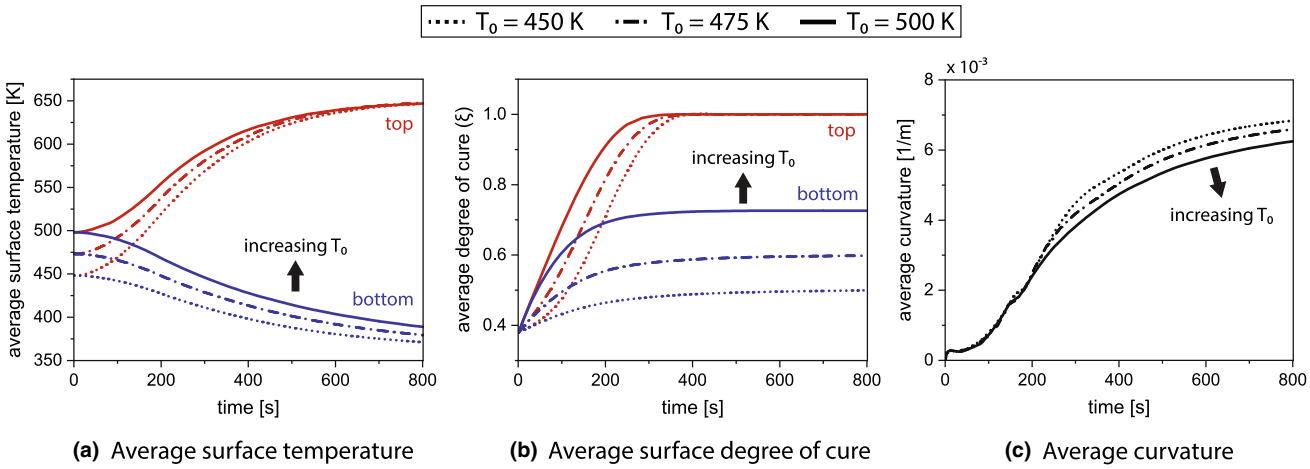

Fig. 9. Effect of the nozzle temperature T_0 on (a) the average surface temperature, (b) average surface degree of cure, and (c) curvature of an extruding CF/epoxy tube in space. Generally, a higher nozzle temperature decreases curvature after extrusion.

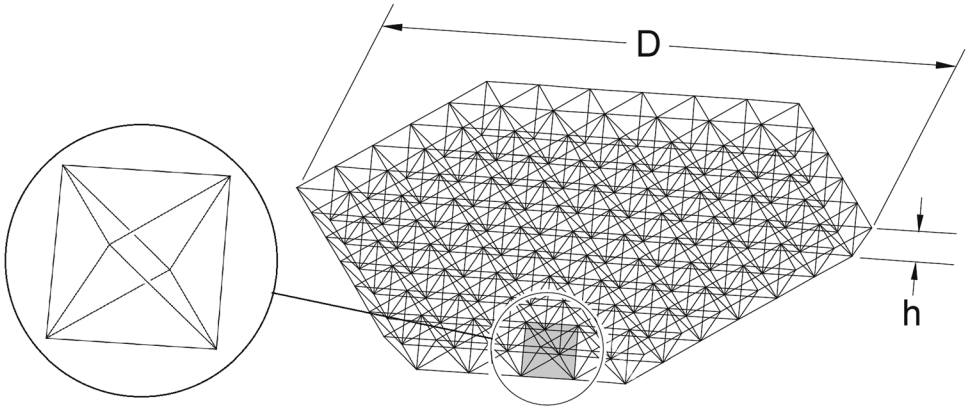

Fig. 10. Tetrahedral truss geometry, adapted from Ref 4. This layered truss structure is made of equal-length struts and is formed by repeating a tetrahedral unit cell to create rings. The resulting structure is hexagonal and supports a flat, faceted reflector.

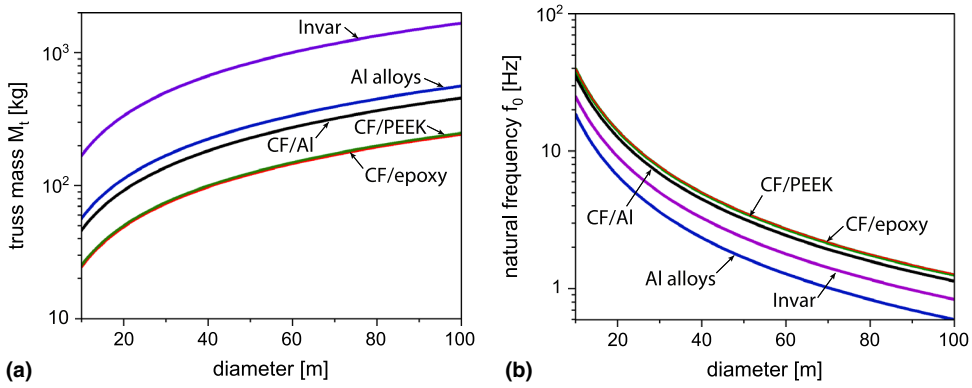

Fig. 11. (a) Approximate mass of a tetrahedral truss as a function of diameter between 10 m and 100 m, plotted for five candidate ISM feedstock materials. CFRP feedstocks yield the lowest truss mass, followed by aluminum-matrix composites and metals. (b) Truss fundamental frequency as a function of diameter. CFRP feedstocks yield the highest natural frequencies.

metric, as the higher Young's modulus of Invar compensates for its higher density.

The third performance metric, total build time, relates to the specific energies discussed in Section 4 and differs for the type of process used to fabricate the tetrahedral truss. For melt-based additive manufacturing and extrusion processes, the total build time $t_{m,e}$ is directly proportional to the truss mass since all the struts are melted or cured during fabrication. Hence, inverting

the build rate given by Eq 9 and multiplying by the truss mass M_t, the total build time for melt-based and extrusion processes is

$$t_{m,e} = \frac{uM_t}{P}, \quad \text{(Eq 20)}$$

where u is the specific process energy and P is the power delivered by the spacecraft. Equation 20 assumes that the build rate is only limited by the power available on orbit.

For processes which feed and deform wire or rod feedstock into truss structures (such as the Bend-Forming process described in Ref 42), the build time t_d depends on the machine feed rate v_f, the total arclength of feedstock L_{tot}, and the total mass of deformed material M_d, which is concentrated at the truss nodes. In this case, the build time can be approximated as

$$t_d = \frac{uM_d}{P} + \frac{L_{tot}}{v_f}. \quad \text{(Eq 21)}$$

For the given tetrahedral truss, expressions for M_d and L_{tot} are derived in Appendix A. Since the tetrahedral truss has straight members, the amount of deformed material is a small fraction of the truss mass ($M_d \ll M_t$), and most of the building time comes from feeding the material to the machine.

By evaluating Eq 20 and 21, we now compare build times as a function of truss diameter, for various materials and manufacturing processes. We assume a constant strut radius of $r = 5$ mm and a fixed output of $P = 1$ kW, which corresponds to the solar panel output of a medium-sized spacecraft. Additionally, for deformation processes, we use a feeding velocity of $v_f = 1.5$ m/min, a typical feeding velocity for an exemplar CNC wire bending machine (Ref 56). With these parameters, we plot in Fig. 12 the total build time as a function of reflector diameter, for the same five candidate materials and their corresponding ISM processes.

Figure 12 highlights the large differences in build time between melting/extrusion and deformation processes. The total build time of the tetrahedral truss with deformation processing of Invar is between several hours and a day, whereas it increases to about 10 days for extrusion of CF/PEEK and up to 50 days for melt-based processing of aluminum alloys. In practice, however, many factors may decrease the build rate for deformation processes. This simple calculation, for instance, does not consider the time required to connect structural components, or the effects of orbital mechanics during fabrication in space.

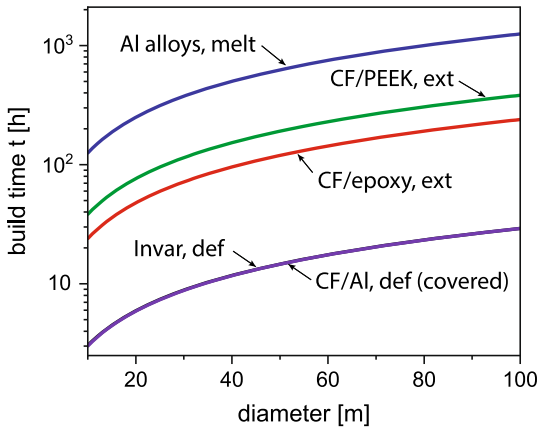

Fig. 12. Approximate build times of a tetrahedral truss as a function of diameter, for various candidate ISM materials and processes. Deformation processes (denoted by def) generally achieve faster build times than extrusion (ext) or melting (melt) processes due to lower specific energy consumption. Note that while the specific energies required to deform Invar and CF/Al are different, their build time is similar since it is dominated by the time spent feeding material, which we model in Eq 21 as independent of the feedstock material.

The above analysis, specific to the tetrahedral truss architecture shown in Fig. 10, suggests that deformation processing can enable dramatically faster build times than extrusion and melt-based processes. However, the current materials compatible with deformation processes yield structures which have lower mass efficiency than those made from carbon fiber-reinforced plastics. Given this tradeoff and the high thermal stability required for precision, deformation processing of carbon fiber-reinforced aluminum appears to be a promising approach for constructing trusses in space. Since carbon fibers have low strain to failure, the feedstock and process would need to be carefully designed to avoid failure during forming.

6. Conclusion

In-space manufacturing shows great promise for the construction of large space structures which can increase the capabilities of communication satellites, enable greater power generation, and support human space exploration. The analysis presented in this study suggests specific materials and approaches for in-space manufacturing as well as key opportunities for further research and development. Material selection for ISM based on three performance metrics important for a large space structure—thermal stability, resistance to disturbances, and minimal-mass buckling strength—highlights several candidate feedstock materials, such as carbon fiber-reinforced aluminum for high thermal stability, carbon fiber-reinforced plastics for minimizing distortion, and beryllium for minimal-mass buckling. However, there is no one material which maximizes all three metrics, motivating the development of hybrid feedstock materials and multi-material ISM to achieve greater structural performance.

The performance of proposed ISM processes (i.e., melt-based processing, extrusion processing, and deformation processing) for constructing structures from these feedstock materials was assessed through a comparison of their respective energy consumption and potential sources of inaccuracies, two important metrics for a fast and accurate ISM approach. Approximate expressions for the specific energy consumption of each process showed that deformation processing requires between 5 and 10 times less energy than both melt-based and extrusion processing (i.e., <1 MJ/kg compared to 5-10 MJ/kg). Therefore, for the same amount of power available on orbit, deformation processing allows for dramatically faster build times. Furthermore, consideration of the unique challenges particular to the space environment illustrates potential issues with achieving accurate structures via processes involving large thermal excursions. For melt-based processes, solar heating and microgravity complicate material deposition, while for extrusion processes, thermomechanical effects such as uneven chemical shrinkage may cause curvature to develop during curing, as demonstrated with a finite element model of an extruding CF/epoxy tube. Since deformation processes do not

require heating of feedstock, their accuracy may be less sensitive to temperature variations and instead depend purely on mechanical sources (e.g., elastic springback).

The relative advantages of these different processes and materials were emphasized through a case study, presented in Section 5, of in-space manufacturing of a tetrahedral truss supporting a reflector surface. Comparing candidate feedstock materials and manufacturing processes for this application showed that deformation processing can achieve build times as low as a day for a 100 m truss, while extrusion processes require build times close to a week. However, feedstock materials amenable to extrusion processes result in higher structural efficiencies, reducing the total truss mass by a factor of three compared to deformation processes.

These results, considered together, show that deformation processing is a promising method of construction in space due to its low energy consumption and potential for high accuracy. While early concepts for deformation processing (Ref 13, 14) have not been implemented on orbit due to challenges with achieving robust joints and geometrically complex structures, with resurgent interest in ISM today and advancements in controls and robotics, we believe deformation processes are worth revisiting. For their successful application in space, automated processes need to be developed which are amenable to forming multi-material feedstock and to the varying thermal environment of space. In addition, an understanding is needed of the orbital mechanics during fabrication, as large changes in center of mass and moment of inertia during forming may affect the attitude and stability of the spacecraft.

Acknowledgments

The authors gratefully acknowledge financial support from Northrop Grumman and the Advanced Concepts Committee at MIT Lincoln Laboratory. The images used in Fig. 2-5 are courtesy of ANSYS, Inc, and the images used in Fig. 7 are courtesy of COMSOL, Inc.

Funding

Open Access funding provided by the MIT Libraries.

Appendix A: Mass Calculations for In-space Manufacturing of a Tetrahedral Truss

For the analysis in Section 5 on the tetrahedral truss shown in Fig. 10, expressions for truss mass M_t, fundamental natural frequency f_0, mass of deformed material M_d, and arclength of feedstock L_{tot} are presented here. For simplicity, each truss member is assumed to be a straight strut with circular cross section, and the nodal joints are assumed to be massless pin connections. Note that some of the equations presented below are results from an earlier study by Lake et al. (Ref 4) on an identical truss geometry.

The mass of a tetrahedral truss with corner-to-corner diameter D and depth h is

$$M_t = \pi\sqrt{\frac{3}{2}}h\rho r^2 N_{\text{struts}}, \tag{Eq A1}$$

where ρ is the strut density, r the strut radius, and N_{struts} the total number of struts, given by (Ref 4)

$$N_{\text{struts}} \approx \frac{13}{3}\left(\frac{D}{h}\right)^2. \tag{Eq A2}$$

The fundamental free-free vibration frequency of the tetrahedral truss is approximated as (Ref 4)

$$f_0 = 0.852\frac{h}{D^2}\sqrt{\eta\frac{E}{\rho}}, \tag{Eq A3}$$

where E is the strut Young's modulus and η is the truss mass fraction, defined as

$$\eta = \frac{\text{truss mass}}{\text{total mass}} = \frac{M_t}{M_t + M_r}. \tag{Eq A4}$$

Here M_t is the truss mass given in (A1) and M_r is the hexagonal reflector mass, approximated with areal density ρ_A as

$$M_r = \frac{3\sqrt{3}}{8}\rho_A D^2. \tag{Eq A5}$$

For fixed D and f_0, (A3) shows that an increase in depth-to-diameter ratio decreases the mass fraction, resulting in increased efficiency. However, above the critical ratio of 0.2, the truss can no longer be modeled as a thin plate and (A3) becomes invalid (Ref 4). Hence, for simplicity, we choose geometries with a fixed depth-to-diameter ratio of 0.2. With this chosen ratio and the areal density of $\rho_A = 18\ \text{kg/m}^2$ specified in Section 5, (A1) and (A3) can be expressed as functions of diameter for various feedstock materials of interest.

For deformation processes, assuming the length of deformed material at each node is equal to the strut diameter, the mass of deformed material is given by:

$$M_d = 2\pi\rho r^3 N_{\text{struts}}. \tag{Eq A6}$$

Assuming the total arclength of feedstock equals the total length of struts,

$$L_{\text{tot}} = N_{\text{struts}}\sqrt{\frac{3}{2}}h. \tag{Eq A7}$$

References

1. R.V. Powell, "A Future for Large Space Antennas," *7th Communications Satellite Systems Conference*, April 24–27, 1978 (San Diego, CA), AIAA, 1978, p 407–414
2. J.M. Hedgepeth and L.R. Adams, "*Design Concepts for Large Reflector Antenna Structures*," 1983, NASA Contractor Report 3663
3. R.A. Russell, T.G. Campbell, and R.E. Freeland, "A Technology Development Program for Large Space Antennas," *Inter. Astronautical Congr. of the Intern. Astronautical Federation*, September 22–29, 1980 (Tokyo, Japan), NASA Technical Memorandum 81902
4. M.S. Lake, L.D. Peterson, and M.B. Levine, Rationale for Defining Structural Requirements for Large Space Telescopes, *J. Spacecr. Rocket.*, 2002, **39**(5), p 674–681. https://doi.org/10.2514/2.3889
5. P.E. Glaser, Power from the Sun: Its Future, *Science*, 1968, **162**, p 857–861. https://doi.org/10.1126/science.162.3856.857
6. R.H. MacNeal, J.M. Hedgepeth, and H.U. Schuerch, "*Heliogyro Solar Sailer Summary Report*," 1969, NASA Contractor Report 1329
7. B.H. Lambrigtsen, S.T. Brown, S.J. Dinardo, T.C. Gaier, P.P. Kangaslahti, and A.B. Tanner, "GeoSTAR: A Geostationary Microwave Sounder for the Future," *Proc. SPIE 6677, Earth Observing Systems XII*, September 27, 2007 (San Diego, CA), SPIE, 2007, p 66771B. https://doi.org/10.1117/12.731933
8. M. Arya, N. Lee, and S. Pellegrino, "Ultralight Structures for Space Solar Power Satellites," *3rd AIAA Spacecraft Structures Conference*, January 4–8, 2016 (San Diego, CA), AIAA, 2016. https://doi.org/10.2514/6.2016-1950
9. H.L. Eaker, "*Significant Electronic Applications and Experimental Results from Project Echo*," WESCON/65, August 24–27, 1965 (San Francisco, CA), NASA Technical Memorandum X-733-65-448
10. R.E. Freeland, G.D. Bilyeu, G.R. Veal, M.D. Steiner, and D.E. Carson, Large Inflatable Deployable Antenna Flight Experiment Results, *Acta Astronaut.*, 1997, **41**(4), p 267–277. https://doi.org/10.1016/S0094-5765(98)00057-5
11. J.F. Garibotti, A.J. Cwiertny, and R. Johnson, On Orbit Fabrication and Assembly of Large Space Structural Subsystems, *Acta Astronaut.*, 1980, **7**(7), p 847–865. https://doi.org/10.1016/0094-5765(80)90075-2
12. J.J. Watson, T.J. Collins, and H.G. Bush, "A History of Astronaut Construction of Large Space Structures at NASA Langley Research Center," *Proc. IEEE Aerospace Conference*, March 9–16, 2002 (Big Sky, MT), IEEE, 2002, 7-3569–7-3587. https://doi.org/10.1109/AERO.2002.1035334
13. Grumman Aerospace Corp., "*Space Fabrication Demonstration System: Final Report*, Technical Volume," Bethpage, NY, 1979, NASA Report N79-29213
14. L. Browning and J.B. Hunt, "*Space Construction Automated Fabrication Experiment Definition Study (SCAFEDS): Final Report, Volume II, Study Results*," San Diego, 1978, NASA Contractor Report 160288
15. S. Ahmed and J.F. Clemmet. "Requirements, Design and Development of Large Space Antenna Structures," *49th Structures and Materials Panel Meeting,* October 7–12, 1979 (Porz-Wahn, Germany), NATO, 1980
16. T. Murphey, "Historical Perspectives on the Development of Deployable Reflectors," *50th AIAA/ASME/ASCE/AHS/ASC Structures, Structural Dynamics and Materials Conference*, May 4–7, 2009 (Palm Springs, CA), AIAA, 2009. https://doi.org/10.2514/6.2009-2605
17. K. Miura and Y. Miyazaki, Concept of the Tension Truss Antenna, *AIAA J.*, 1990, **28**(6), p 1098–1104. https://doi.org/10.2514/3.25172
18. E.O. Adams and C.N. Irvine, "*MSFC Evaluation of the Space Fabrication Demonstration System (Beam Builder)*," Marshall Space Flight Center, 1981, NASA Technical Memorandum 82440
19. A. Brinkmeyer, S. Pellegrino, and P.M. Weaver, Effects of Long-term Stowage on the Deployment of Bistable Tape Springs, *J. Appl. Mech.*, 2016, **83**(1), 011008. https://doi.org/10.1115/1.4031618
20. J.A. Banik, "Realizing Large Structures in Space," *2015 US Frontiers of Engineering*, September 9–11, 2015 (Irvine, CA), National Academy of Engineering
21. K. Taminger and R.A. Hafley, "Electron Beam Freeform Fabrication: A Rapid Metal Deposition Process," *Proc. 3rd Automotive Composites Conference*, September 9–10, 2003 (Troy, MI), Society of Plastics Engineers, 2003
22. J. Kugler, J. Cherston, E.R. Joyce, P. Shestople, and M.P. Snyder, "Applications for the Archinaut In Space Manufacturing and Assembly Capability," *AIAA SPACE and Astronautics Forum and Exposition*, September 12–14, 2017 (Orlando, FL), AIAA, 2017. https://doi.org/10.2514/6.2017-5365
23. B. Levedahl, R. Hoyt, J. Gorges, T. Silagy, N. Britton, G. Jimmerson, M. Bodnar, and J. Slostad, "Trusselator™ Technology for In-Situ Fabrication of Solar Array Support Structures," *2018 AIAA Spacecraft Structures Conference*, January 8–12, 2018 (Kissimmee, FL), AIAA, 2018. https://doi.org/10.2514/6.2018-2203
24. Kleos Space, "Futurism," https://kleos.space/futrism/. Accessed 4 October 2021
25. J.M. Hedgepeth, Accuracy Potentials for Large Space Antenna Reflectors with Passive Structure, *J. Spacecr. Rocket.*, 1982, **19**(3), p 211–217. https://doi.org/10.2514/3.62239
26. M.M. Mikulas, "*Structural Efficiency of Long Lightly Loaded Truss and Isogrid Columns for Space Applications*," 1978, NASA Technical Memorandum 78687
27. M.F. Ashby, "*Materials Selection in Mechanical Design*," 4th ed., Elsevier Ltd., 2011
28. H.G. Bush, M.M. Mikulas, and W.L. Heard, Some Design Considerations for Large Space Structures, *AIAA J.*, 1978, **16**(4), p 352–359. https://doi.org/10.2514/3.60897
29. D. Cebon and N.F. Ashby, Materials Selection for Precision Instruments, *Meas. Sci. Technol.*, 1994, **5**(3), p 296–306. https://doi.org/10.1088/0957-0233/5/3/014
30. Ansys Granta EduPack software, ANSYS, Inc., Cambridge, UK, 2021
31. H.P. Stahl, L.D. Feinberg, and S.C. Texter, "JWST primary mirror material selection," *Proc. SPIE 5487, Optical, Infrared, and Millimeter Space Telescopes*, October 12, 2004 (Glasgow, UK), SPIE, 2004, p 818–824. https://doi.org/10.1117/12.549582
32. M. Straubel, J. Block, M. Sinapius, and C. Hühne, "Deployable Composite Booms for Various Gossamer Space Structures," *52nd AIAA/ASME/ASCE/AHS/ASC Structures, Structural Dynamics and Materials Conference*, April 4–7, 2011 (Denver, CO), AIAA, 2011. https://doi.org/10.2514/6.2011-2023
33. M.K. Chamberlain, S.H. Kiefer, and J. Banik, "On-orbit structural dynamics performance of the roll-out solar array," *2018 AIAA Spacecraft Structures Conference*, January 8–12, 2018 (Kissimmee, FL), AIAA, 2018. https://doi.org/10.2514/6.2018-1942
34. L. Johnson, M. Whorton, A. Heaton, R. Pinson, G. Laue, and C. Adams, NanoSail-D: A Solar Sail Demonstration Mission, *Acta Astronaut.*, 2011, **68**(5–6), p 571–575. https://doi.org/10.1016/j.actaastro.2010.02.008
35. Materion Corp., "*SupremEX Metal Matrix Composites Improve Precision in Space and Defense Systems*," https://materion.com/products/metal-matrix-composites/supremex/space-defense-and-optical-systems. Accessed 4 October 2021
36. NASA, "*On-Orbit Servicing, Assembly, and Manufacturing 2 (OSAM-2)*," https://www.nasa.gov/mission_pages/tdm/osam-2.html. Accessed 4 October 2021
37. T. Gutowski, S. Jiang, D. Cooper, G. Corman, M. Hausman, J. Manson, T. Schudeleit, K. Wegener, M. Sabelle, J. Ramos-Grez, and D.P. Sekulic, Note on the Rate and Energy Efficiency Limits for Additive Manufacturing: Rate and Energy Efficiency Limits for AM, *J. Ind. Ecol.*, 2017, **21**(S1), p S69–S79. https://doi.org/10.1111/jiec.12664
38. Z. Liu, Q. Jiang, F. Ning, H. Kim, W. Cong, C. Xu, and H. Zhang, Investigation of Energy Requirements and Environmental Performance for Additive Manufacturing Processes, *Sustainability*, 2018, **10**(10), p 3606. https://doi.org/10.3390/su10103606
39. S.W. Tsai and H.T. Hahn, *Introduction to Composite Materials*, Technomic Publishing Co., Inc., Pennsylvania, 1980
40. J.A. Schey, *Introduction to Manufacturing Processes*, McGraw-Hill Inc., New York, 1977
41. A. Deignan, L. Figiel, and M.A. McCarthy,Insights into Complex Rheological Behaviour of Carbon Fibre/PEEK from a Novel Numerical Methodology Incorporating Fibre Friction and Melt Viscosity, *Compos. Struct.*, 2018, **189**, p 614–626. https://doi.org/10.1016/j.compstruct.2018.01.084
42. H.G. Bhundiya, F. Royer, and Z. Cordero, "Compressive behavior of isogrid columns fabricated with bend-forming," *AIAA Scitech 2022 Forum*, January 3–7, 2022 (San Diego, CA), AIAA, 2022. https://doi.org/10.2514/6.2022-2263
43. J.M. Hedgepeth, Influence of Fabrication Tolerances on the Surface Accuracy of Large Antenna Structures, *AIAA J.*, 1982, **20**(5), p 680–686. https://doi.org/10.2514/3.7936

44. A. Boschetto and L. Bottini, Accuracy Prediction in Fused Deposition Modeling, *Int. J. Adv. Manuf. Technol.*, 2014, **73**(5–8), p 913–928. https://doi.org/10.1007/s00170-014-5886-4
45. W.J. Sames, F.A. List, S. Pannala, R.R. Dehoff, and S.S. Babu, The Metallurgy and Processing Science of Metal Additive Manufacturing, *Int. Mater. Rev.*, 2016, **61**(5), p 315–360. https://doi.org/10.1080/09506608.2015.1116649
46. R. Hafley, K. Taminger, and R. Bird, "Electron Beam Freeform Fabrication in the Space Environment," *45th AIAA Aerospace Sciences Meeting and Exhibit*, January 8–11, 2007 (Reno, NV), AIAA, 2007. https://doi.org/10.2514/6.2007-1154
47. K. Minchenkov, A. Vedernikov, A. Safonov, and I. Akhatov, Thermoplastic Pultrusion: A Review, *Polymers*, 2021, **13**(2), p 180. https://doi.org/10.3390/polym13020180
48. C. Ajinjeru, V. Kishore, J. Lindahl, Z. Sudbury, A.A. Hassen, B. Post, L. Love, V. Kunc, and C. Duty, The Influence of Dynamic Rheological Properties on Carbon Fiber-reinforced Polyetherimide for Large-scale Extrusion-based Additive Manufacturing, *Int. J. Adv. Manuf. Technol.*, 2018, **99**(1–4), p 411–418. https://doi.org/10.1007/s00170-018-2510-z
49. S.K. Romberg, M.A. Islam, C.J. Hershey, M. DeVinney, C.E. Duty, V. Kunc, and B.G. Compton, Linking Thermoset Ink Rheology to the Stability of 3D-printed Structures, *Addit. Manuf.*, 2021, **37**, 101621. https://doi.org/10.1016/j.addma.2020.101621
50. COMSOL Multiphysics Reference Manual, v. 5.6, COMSOL, Inc., www.comsol.com
51. O.G. Kravchenko, S.G. Kravchenko, and R.B. Pipes, Chemical and Thermal Shrinkage in Thermosetting Prepreg, *Compos. A Appl. Sci. Manuf.*, 2016, **80**, p 72–81. https://doi.org/10.1016/j.compositesa.2015.10.001
52. H. Yu, S.G. Mhaisalkar, and E.H. Wong, Observations of Gelation and Vitrification of a Thermosetting Resin During the Evolution of Polymerization Shrinkage, *Macromol. Rapid Commun.*, 2005, **26**(18), p 1483–1487. https://doi.org/10.1002/marc.200500333
53. K.J. Yoon and J.S. Kim, Effect of Thermal Deformation and Chemical Shrinkage on the Process Induced Distortion of Carbon/epoxy Curved Laminates, *J. Compos. Mater.*, 2001, **35**(3), p 253–263. https://doi.org/10.1177/002199801772662244
54. W.F. Hosford and R.M. Caddell, *Metal Forming: Mechanics and Metallurgy*, Cambridge University Press, Cambridge, 2011
55. NASA, "Observatory Webb's Mirrors," https://www.jwst.nasa.gov/content/observatory/ote/mirrors/index.html. Accessed 4 October 2021
56. Pensa Labs, "D.I. Wire Pro Datasheet," 2020